Front. Energy 2023, 17(6): 751–762
https://doi.org/10.1007/s11708-023-0895-3

RESEARCH ARTICLE

Yibo GAO, Erjiang HU, Bo HUANG, Zuohua HUANG

Formic acid dehydrogenation reaction on high-performance Pd_xAu_{1-x} alloy nanoparticles prepared by the eco-friendly slow synthesis methodology

Abstract Dehydrogenation of formic acid (FA) is considered to be an effective solution for efficient storage and transport of hydrogen. For decades, highly effective catalysts for this purpose have been widely investigated, but numerous challenges remain. Herein, the Pd_xAu_{1-x} (x = 0, 0.2, 0.4, 0.5, 0.6, 0.8, 1) alloys over the whole composition range were successfully prepared and used to catalyze FA hydrogen production efficiently near room temperature. Small PdAu nanoparticles (5–10 nm) were well-dispersed and supported on the activated carbon to form PdAu solid solution alloys via the eco-friendly slow synthesis methodology. The physicochemical properties of the PdAu alloys were comprehensively studied by utilizing various measurement methods, such as X-ray diffraction (XRD), N_2 adsorption–desorption, high angle annular dark field-scanning transmission electron microscope (HAADF-STEM), X-ray photoelectrons spectroscopy (XPS). Notably, owing to the strong metal-support interaction (SMSI) and electron transfer between active metal Au and Pd, the $Pd_{0.5}Au_{0.5}$ obtained exhibits a turnover frequency (TOF) value of up to 1648 h^{-1} (313 K, n_{Pd+Au}/n_{FA} = 0.01, n_{HCOOH}/n_{HCOONa} = 1:3) with a high activity, selectivity, and reusability in the FA dehydrogenation.

Keywords FA dehydrogenation, face-centred cubic structures, PdAu solid solution alloy nanoparticles, slow synthesis methodology, SMSI effect

Received May 23, 2023; accepted Jul. 6, 2023; online Sept. 16, 2023

Yibo GAO, Erjiang HU (✉), Zuohua HUANG
State Key Laboratory of Multiphase Flow in Power Engineering, Xi'an Jiaotong University, Xi'an 710049, China
E-mail: hujiang@mail.xjtu.edu.cn

Bo HUANG (✉)
Institute of Chemical Engineering and Technology, Xi'an Jiaotong University, Xi'an 712000, China
E-mail: bohuang@mail.xjtu.edu.cn

1 Introduction

Since the 21st century, the world faces two major challenges, energy crisis and environment deterioration. Finding and exploring safe, clean, and renewable energies has become a hot research topic. As an ideal carbon-zero fuel, hydrogen is viewed as the most promising alternatives for changing the traditional fossil energy system because of a variety of advantages (high-efficiency, recyclability, cleanness, etc.) [1,2]. Particularly, H_2 has been widely used in proton exchange membrane fuel cells because its product is only water [3]. Chemical hydrogen storage materials are widely preferred due to their high weight and volumetric hydrogen density compared to classical pressurization and cryogenic liquefaction technologies [4,5]. For decades, the chemical H_2 storage materials: formic acid (FA, HCOOH) [6,7], methanol (CH_3OH) [8,9], sodium borohydride ($NaBH_4$) [10,11], hydrazine (N_2H_4) [12,13], hydrous hydrazine ($N_2H_4{\cdot}H_2O$) [14–16], and hydrazine borane (NH_3BH_3) [17,18] have been comprehensively investigated and developed for transportation and generation of hydrogen [19,20].

As one of the common liquid biomass products, formic acid (FA) possesses a relatively high hydrogen storage content, density, and volume. Therefore, it has received widespread attention in the application of portable hydrogen storage devices because of its low price, chemical stability, and easy storage and transportation [7,21,22]. Moreover, it is easily charged and discharged through sharing current infrastructures of liquid fuels, which greatly promotes its production and application. As the reverse reaction of CO_2 hydrogenation [23,24], it can be decomposed into H_2 and CO_2 by dehydrogenation (HCOOH → CO_2 + H_2, ΔG_{298} = −48.4 kJ/mol) or by dehydration (HCOOH → CO + H_2O, ΔG_{298} = −28.5 kJ/mol), but the last is undesirable because CO can poison the catalysts in fuel cells [25,26]. Therefore, rapid

development of highly active catalysts accompanied with high selectivity and efficient H_2 generation is of paramount for FA-based hydrogen storage.

Many works have been made to investigate the homogeneous and heterogeneous catalysts in FA hydrogenation. For homogeneous catalysts, Schneider and its coworkers [27] reported that ($^{iPr}PN^{H}P$)Fe(CO)H-(COO) and Lewis acid cocatalyst obtain an particularly high turnover frequency (TOF) value of 196728 h^{-1} at 353 K. However, homogeneous catalysts still face many problems such as special additives, separation, and recovery, which further limit the practical application of catalysts. To date, a large number of researchers have explored the heterogeneous catalysts for FA dehydrogenation. As the most competitive catalyst for FA hydrogenation, Pd-based catalysts have high activities and median adsorption energy values compared to other metal-based catalysts [4,28–30]. But Pd-based single metal catalyst exhibit an acceptable H_2 generation rate at a relatively high temperature (333–433 K) accompany with the addition of sodium and potassium salts. Additionally, the production of CO byproducts could cause the inactivation of mono-metal Pd-based catalyst [29,31–37]. Therefore, many Pd-based binary and ternary metal (PdAu [38–44], PdAg [45–47], PdCu [5], PdCo [48], PdAuCo [49], PdAgCo [50] and PdAu-MnO_x [51,52]) catalysts exhibit a higher reactivity as well as reusability compared with Pd mono-metal catalysts. Although Au alone is inactive for FA decomposition, PdAu [53,54] bimetal catalysts could greatly enhance the catalytic performance due to their synergistic effect. The charge transfer between Au and Pd not only plays an important role in regulating the chemical environment nearby the active center Pd, but also inhibits the generation of CO and prevents catalysts poisoning [55,56]. Moreover, many significant works are employed to increase the structure-reactivity relationship of PdAu bimetal catalysts including alloy structures [38,57], core shell structures [58], and contracture strong metal-support interaction (SMSI). For the abovementioned several structures, the uniformly mixing PdAu bimetals with smaller particle sizes poses a huge challenge [59,60], directly affecting the FA dehydrogenation activity.

Recently, new ultra-small solid-solution alloys have been synthesized, which aroused lots of attention due to their many innovative properties [61,62]. The greatest advantage of solid solution alloys is the control of their electronic structure at the atomic level in the bulk state and the influence of most physicochemical properties via altering the metals compositions in the solution [63]. By completely mixing of metals A and B, the AB alloy possesses not only the properties of A or B, but also a unique property because of the synergistic capacity of A and B. Although many immiscible alloys including PdAu [64], CuRu [65], RhNi [66], AuRu [63], etc. have been prepared, the synthesis of solid solution alloys nanoparticles (NPs) with large differences in reduction potential remains challenging. For noble metal alloy NPs, the most critical control step is the co-reduction rate of double metals, otherwise core shell or isolated single metal NPs can be obtained [67,68]. Hence, it is challenging to co-reduce bimetal ions with a large gap in reduction potential energy. The reduction potentials are shown in Table S1 in Electronic Supplementary Material. Difference in the reduction rates including Au and Pd that possess the large gap in noble metals ($Pd^{2+} + 2e^- \rightarrow Pd$, $E^0 = 0.951$ V vs. $Au^{3+} + 3e^- \rightarrow Au$, $E^0 = 1.498$ V) [63,69].

In this work, the slow synthesis methodology was carefully adopted to synthesize PdAu solid solution alloy so that all components are distributed randomly and homogeneously. Based on this idea, activated carbon (AC) with a developed porous structure was used as basic support to deposit ultrafine Pd_xAu_{1-x} (x = 0, 0.2, 0.4, 0.5, 0.6, 0.8, 1) solid solution alloy NPs. PdAu alloy NPs were successfully obtained and catalyzed FA dehydrogenation. By regulating various composition ratios, the optimal $Pd_{0.5}Au_{0.5}$ catalyst exhibits the highest activity (TOF = 1648 h^{-1}) for HCOOH/HCOONa (formic acid/formate (FA/SF)) dehydrogenation at 313 K. Furthermore, reaction temperature, FA/SF ratios, metal loading quantity and stability of catalysts were also tested.

2 Experiment

2.1 Chemicals

The Na_2PdCl_4 (99% purity), $HAuCl_4 \cdot 3H_2O$ (99% purity), $NaBH_4$ (98% purity), HCOOH (88% purity), and HCOONa (99.5% purity) were obtained from Aladdin Chemistry Co., Ltd., while the AC was obtained from Macklin Chemicals Co., Ltd. All the chemicals were not further purified.

2.2 Catalyst characterizations

The crystal structures of PdAu alloy NPs were detected via XRD using a SHIMADZU XRD-6000 with Cu Kα radiation (λ = 0.15406 nm). The 2θ data from 30° to 90° were 0.02°-intervals. The physical properties of catalysts including S_{BET} (m^2/g), V_p (cm^3/g), and D_p (nm) were determined using the nitrogen-sorption method on a constant volume adsorption equipment (Micrometrics ASAP 2020 Plus HD88, USA). The pore volume was analyzed by the Barrett-Joyner-Halenda (BJH). The microstructure and morphology were tested by the HAADF-STEM and EDX-mapping on the Thermo Scientific Talos-F200X. Thermo Scientific K-Alpha with monochromatic Al K-Alpha (1486.7 eV) was carried to record X-ray photoelectron spectroscopy. The atomic ratios of Pd and Au was recorded using an inductively

coupled plasma mass spectroscopy (ICP-MS) on a NexION^{TM} 350D instrument (PerkinElmer, USA).

2.3 Catalyst preparation

As shown in Fig. 1, the Pd_xAu_{1-x} (x = 0, 0.2, 0.4, 0.5, 0.6, 0.8, 1) alloy NPs with an appropriate composition and a metal loading of 5% were prepared. Taking $Pd_{0.5}Au_{0.5}$ synthesis as an example, Na_2PdCl_4 (29 mg, 0.1 mmol) and $HAuCl_4{\cdot}3H_2O$ (0.1 mmol) were added in 60 mL H_2O and stirred for 30 min as metal precursor solutions. $NaBH_4$ (152 mg, 4 mmol) was added in 60 mL ethyleneglycol (EG). AC (580 mg) was dissolved in 100 mL H_2O. After that, the metal precursor solution and EG solution were added dropwise to the AC mixed solution at a rate of 1.2 mL/min [70]. After the dropping process, the mixed solution was stirred for 30 min. The sediment obtained was collected by centrifugation and washed over 5 times with H_2O. The sediment collected by centrifugation was washed with H_2O for 5 times. Finally, the product was dried at 60 °C under vacuum. The Pd_xAu_{1-x} (x = 0, 0.2, 0.4, 0.6, 0.8, 1) alloy NPs and x% $Pd_{0.5}Au_{0.5}$ (x = 1, 5, 10) with different metal loadings were also obtained by altering the atomic ratios of Pd^{2+} and Au^{2+}.

2.4 Catalyst evaluation

The synthesized catalyst was dispersed in deionized water in a round-bottomed flask and placed in a water bath at the preset temperature. Flask was connected to a reflux and a gas dropped where the gas produced from the FA dehydrogenation was collected. Subsequently, FA/SF in a certain molar ratio (1:3, 2:3, 1:8, 1:1, 3:2, and 3:1) was injected to the flask and started to react with vigorous stirring. Moreover, the activation energy (E_a) of reaction was calculated by conducting the catalytic reaction over a temperature range of 293–313 K. From the slope of each line, the rate constants K were obtained at preset temperatures. Finally, the TOF values were obtained using Eq. (1).

$$\mathrm{TOF} = \frac{P_{\mathrm{atm}} V_{\mathrm{gas}}}{RT} / (n_{\mathrm{PdAu}} \cdot t), \quad (1)$$

where P_{atm} is the atmospheric pressure (101325 Pa), V_{gas} is the gas volume produced from the FA dehydrogenation reaction which has reached 20%, R is the universal gas constant, T is preset temperature (313 K), n_{PdAu} is the total mole amount of PdAu atoms, and t is FA decomposition time (min). Based on ICP-MS analyses, the total mole amount of PdAu atoms on the AC are shown in Table S2.

3 Results and discussion

3.1 XRD

To investigate the structures of the Pd_xAu_{1-x} (x = 0, 0.2, 0.4, 0.5, 0.6, 0.8, 1) alloy NPs, the XRD patterns were obtained as shown in Fig. 2. The lattice constants and crystal sizes of all the PdAu NPs were summarized in Table 1. For Au NPs, apparent diffraction peaks appear at 38.3°, 44.3°, 64.7°, and 77.7° are assigned to the (111), (200), (220) and (331) planes of the fcc-Au (JCPDS No. 65-8601), showing the structural formation of Au NPs. Compared to the Au NPs, the diffraction peaks of Pd NPs are weaker, exhibiting that the particle size of Pd NPs should be smaller. With the increase in Au mixing content, the diffraction peaks of Pd_xAu_{1-x} alloy NPs shift to lower Bragg angles (Fig. 2), but remain between the fcc-Au and fcc-Pd (JCPDS No. 05-0681) phases. According to the nominal composition, the Pd and Au atoms are randomly attributed to each lattice site. The lattice constant and crystal size of PdAu alloys decrease significantly with the mixing of palladium because of the smaller ionic radii of Pd compared to those of Au (Table 1). These obvious characterizations, including lattice constant, diffraction peaks shift, and mean crystal size, strongly suggest the formations of the Pd_xAu_{1-x} (x = 0, 0.2, 0.4, 0.5, 0.6, 0.8, 1) alloys in the whole composition range.

3.2 N_2 adsorption/desorption measurements

N_2 sorption isotherms and corresponding pore size distributions plot for PdAu alloys are shown in Fig. 3. All PdAu alloy NPs exhibit typical IV isotherms with H1 hysteresis loops, which is characteristic of mesoporous

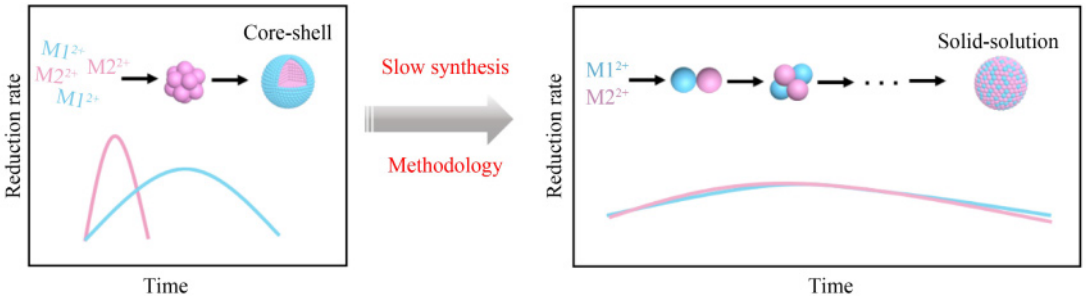

Fig. 1 Schematic images of slow synthesis methodology in PdAu alloy systems.

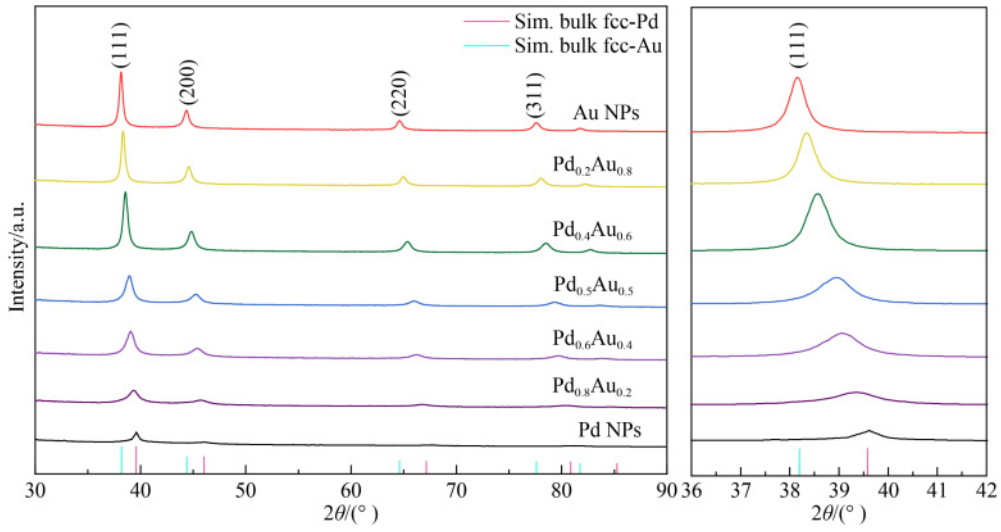

Fig. 2 XRD patterns of PdAu alloys and the simulated XRD patterns of fcc-Pd and fcc-Au.

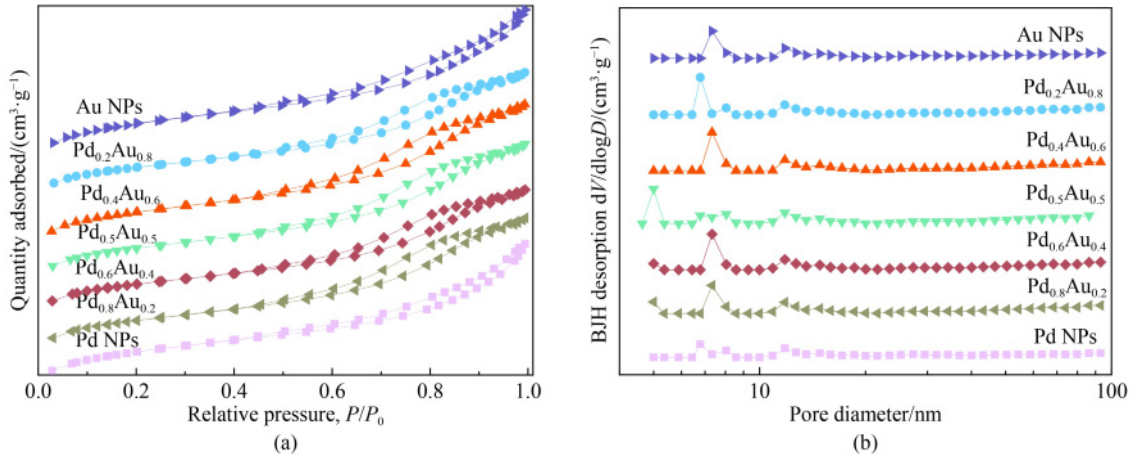

Fig. 3 (a) N_2 adsorption–desorption isotherms and (b) BJH pore distribution obtained from Pd_xAu_{1-x} alloy NPs.

Table 1 Structural characteristics of the synthesized samples

Samples	$2\theta^a$/(°)	a^b/Å	X_s^c/nm	S_{BET}^d/(m^2·g^{-1})	V_p^e/(cm^3·g^{-1})	D_p^f/nm
Au NPs	38.20	4.08078	8.87	950.4	0.514	6.3
$Pd_{0.2}Au_{0.8}$	38.32	4.03918	7.12	992.5	0.540	6.1
$Pd_{0.4}Au_{0.6}$	38.56	4.00528	6.99	1054.8	0.568	6.3
$Pd_{0.5}Au_{0.5}$	38.96	3.98761	6.23	360.4	0.622	5.3
$Pd_{0.6}Au_{0.4}$	39.12	3.95827	5.60	1027.8	0.617	6.2
$Pd_{0.8}Au_{0.2}$	39.37	3.89076	4.28	1044.2	0.556	6.3
Pd NPs	39.62	3.88636	4.00	825.3	0.584	6.4

Notes: *a* is the (111) crystal face, *b* is the Lattice constant, *c* is the crystal size, *d* is the specific surface area of N_2 adsorption–desorption, *e* is the total pore volume, and *f* is the average pore diameter.

structure. The values of S_{BET}, V_p, and D_p of all the PdAu alloy NPs are listed in Table 1. The AC support used provides a large specific surface area for the anchorage of the PdAu alloy. The surface area (1166 m^2/g) and total pore volume (0.622 cm^3/g) of $Pd_{0.5}Au_{0.5}$ far outperform those of other PdAu alloy NPs. When the Pd/Au ions ratio is unequal, the total pore volume and specific surface area decrease significantly. Such a reduction may be related to the aggregation of larger PdAu alloy NPs blocking pores and/or causing some structural rearrangements

[71]. In general, the large surface and high porosity of PdAu alloys facilitate the active point between catalyst and FA, thus promoting FA dehydrogenation.

3.3 High angle annular dark field-scanning transmission electron microscope (HAADF-STEM)

The synthesized PdAu alloy NPs were characterized by HAADF-STEM analysis. The mean diameter of the Pd_xAu_{1-x} (x = 0, 0.2, 0.4, 0.5, 0.6, 0.8, 1) alloy NPs were 10.9, 8.1, 7.3, 6.7, 6.5, 5.9, and 6.3 nm, respectively (Figs. 4 and S1). These particle sizes were measured by averaging at least 100 nanoparticles. The mean particle sizes of Au NPs are relatively larger than that of other Pd_xAu_{1-x} (x = 0.2, 0.4, 0.5, 0.6, 0.8, 1) NPs. This may be related to the fast nucleating nature of Au [61]. From the ICP-MS analysis, the atomic ratios of Pd and Au in alloys, shown in Table S2, were in consistent with the original ratios.

To clarify the Pd and Au ions of the mixing state in the

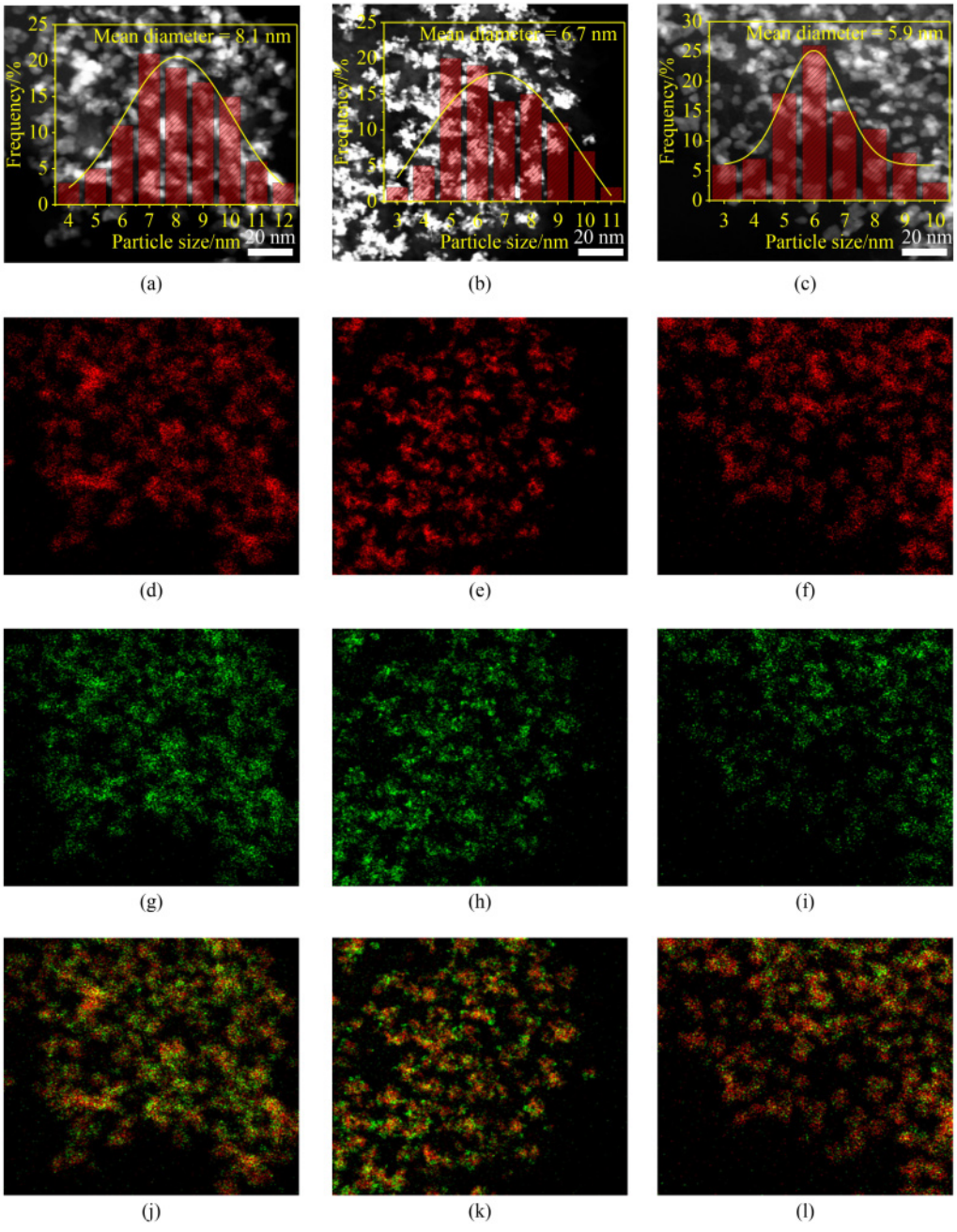

Fig. 4 HAADF-STEM images

(a) $Pd_{0.2}Au_{0.8}$; (b) $Pd_{0.5}Au_{0.5}$; (c) $Pd_{0.8}Au_{0.2}$ NPs; (d–f) corresponding Pd-L, Au-L, and overlay STEM EDX maps of (a); (g–i) corresponding Pd-L, Au-L, and overlay STEM EDX maps of (b); (j–l) corresponding Pd-L, Au-L, and overlay STEM EDX maps of (c).

Pd_xAu_{1-x} alloy NPs, STEM EDX mappings of Pd-L and Au-L were performed. In Figs. 4 and S2, the elemental maps of Pd and Au show that the two elements are randomly and homogeneously distributed in the whole area of NPs. The EDX line-scan profiles are shown in Figs. 5 and S3, which indicate that the metal composition is transferred from Au-rich to Pd-rich. The Pd and Au ratios based on the EDX area-scan data are also listed in Table S2, which agree well with the theoretical Pd/Au atomic ratios in preparation. The EDX analysis suggests that the Pd/Au atomic ratios in the $Pd_{0.5}Au_{0.5}$ NPs is 49.3:50.7.

3.4 XPS measurements

As shown in Fig. 6, the chemical states and surface electronic properties of the Pd_xAu_{1-x} (x = 0, 0.2, 0.4, 0.5, 0.6, 0.8, 1) alloy NPs were investigated via X-ray photoelectron spectra. The remarkable XPS peaks of C 1s for PdAu alloy NPs at 284.8 and 286.4 eV are shown in Fig. S4 and assigned to the C–C/C=C and C–O, respectively [4,72]. Meanwhile, $Pd_{0.2}Au_{0.8}$ (Pd^0 $3d_{3/2}$ at 341.3 eV and Pd^0 $3d_{5/2}$ at 336.0 eV) possesses a higher BEs of Pd^0 $3d_{3/2}$ (340.9 eV) and Pd^0 $3d_{5/2}$ (335.9 eV) for Pd_xAu_{1-x} (x = 0.4, 0.5, 0.6, 0.8, 1) alloy NPs. The deviation of BEs in the direction of high energy indicate that there exists an SMSI effect between PdAu and AC due to the introduction of Au [73]. In addition, the other two peaks at 343.3 and 337.5/338.2 eV is expected to Pd^{2+} $3d_{3/2}$ and Pd^{2+} $3d_{5/2}$. This may be caused by electronic interactions between the Pd d-orbitals and AC [74,75]. Au^0 4f binding energies for the Pd_xAu_{1-x} (x = 0.2, 0.4, 0.5, 0.6, 0.8) shift lower values compared to those of Au NPs (87.9 and 84.3 eV). The above XPS spectra of Pd 3d and electronegativity difference for Pd (2.2) and Au (2.4) also demonstrate that Pd loses a few electrons to Au in PdAu alloys. For the $Pd_{0.5}Au_{0.5}$, the BEs for Au^0 4f are located at 87.8 and 84.2 eV. The XPS results indicate that there exists an SMSI effect between PdAu alloy and AC. It is worth noting that Pd 3d and Au 4f binding energy shift positively as the Au content increasing. The BEs of Pd/Au ratio is related to the interactions between Pd and Au. Due to the formation of non-homogeneous junctions in the electronic structure of Pd and the SMSI effect [76], the adsorption of formate can be enhanced from electron-rich Pd. These phenomena remarkably enhance the catalytic FA dehydrogenation [38,72].

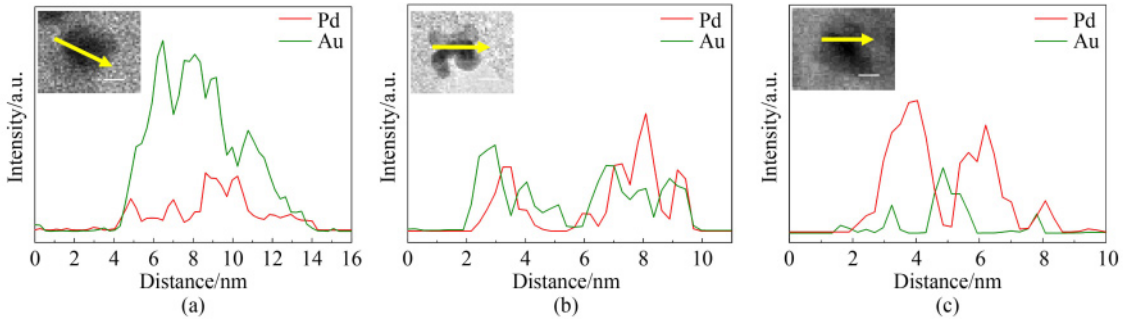

Fig. 5 EDX line graphs of NPs (Pd and Au are indicated in red and green colors and scale bars are 5 nm).
(a) EDX line graphs of NPs shown along the arrows in inset of $Pd_{0.2}Au_{0.8}$; (b) EDX line graphs of NPs shown along the arrows in inset of $Pd_{0.5}Au_{0.5}$; (c) EDX line graphs of NPs shown along the arrows in inset of $Pd_{0.8}Au_{0.2}$ NPs.

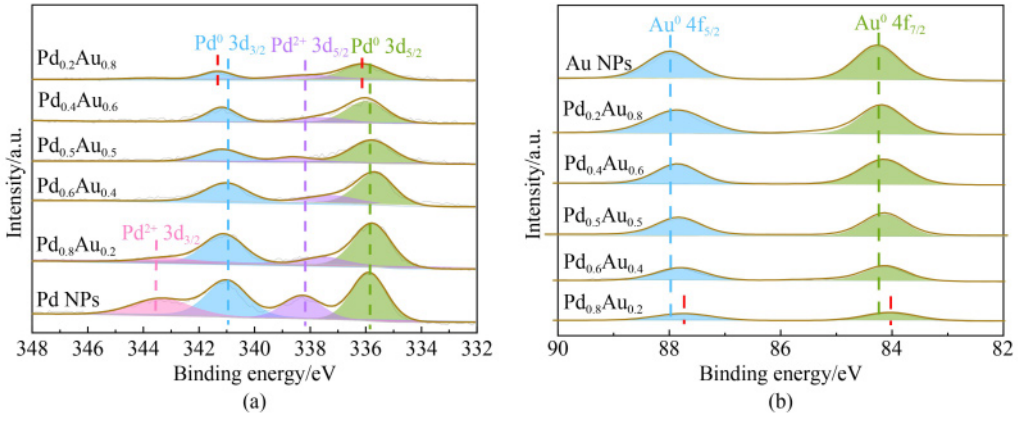

Fig. 6 (a) Pd 3d and (b) Au 4f XPS spectra on Pd_xAu_{1-x} (x = 0, 0.2, 0.4, 0.5, 0.6, 0.8, 1) alloys.

3.5 FA dehydrogenation in FA/SF solution

Catalytic performances over the Pd_xAu_{1-x} (x = 0, 0.2, 0.4, 0.5, 0.6, 0.8, 1) alloys obtained toward the FA dehydrogenation with SF were measured in a burette system. The AC support and Au NPs showed a poor hydrogenation production (Fig. 7(a)). As a synergistic promoter of metals, the contribution of Au to the decomposition of FA is assigned to the SMSI effect at the heterogeneous interfaces between the PdAu alloy and the AC support. As shown in Figs. 7(a) and S5, the $Pd_{0.5}Au_{0.5}$ has the highest catalytic activity (TOF = 1648 h^{-1}) of all the Pd_xAu_{1-x} (x = 0, 0.2, 0.4, 0.6, 0.8, 1) NPs. The excellent catalytic performance of $Pd_{0.5}Au_{0.5}$ due to the ultrafine and polydispersity PdAu NPs on the surface of AC and electrons transfer efficiently from Pd to Au over PdAu alloy NPs. Meanwhile, the large specific surface area of AC also improves the dispersion of active metal sites, allowing for a greater exposure to the FA dehydrogenation. Moreover, Au doping allows the Pd to be the electron-state, thus enhancing the catalytic performances for FA decomposition efficiently. In FA decomposition, SF is used as an accelerator to increase the reaction activity of hydrogen evolution reaction [19,77]. The generated gas compositions from the aqueous FA/SF solution over the $Pd_{0.5}Au_{0.5}$ are shown in Fig. S6. The optimal ratio of FA/SF for $Pd_{0.5}Au_{0.5}$ is 1:3 at 313 K and it showed a conversion of around 100% for FA decomposition near room temperature (Figs. 7(c) and S6). Additionally, optimum metal loading of PdAu on the AC is 5 wt.% (mass fraction) in FA dehydrogenation (Fig. 7(d)).

The Arrhenius plot and corresponding kinetic parameters over $Pd_{0.5}Au_{0.5}$ and Pd NPs catalysts were shown in Figs. 7(b) and S7. Through the $V_{H_2+CO_2}$ rate versus time, the Arrhenius plot shows a slope of −6.8144, indicating that FA decomposition is nearly a first order reaction relative to the reaction temperature. In addition, the apparent activation energy (E_a) for Pd NPs and $Pd_{0.5}Au_{0.5}$ alloy NPs of FA/SF is obtained from 293 to 313 K. The above analysis indicates that the rate of H_2 production increases with rising reaction temperature. According to

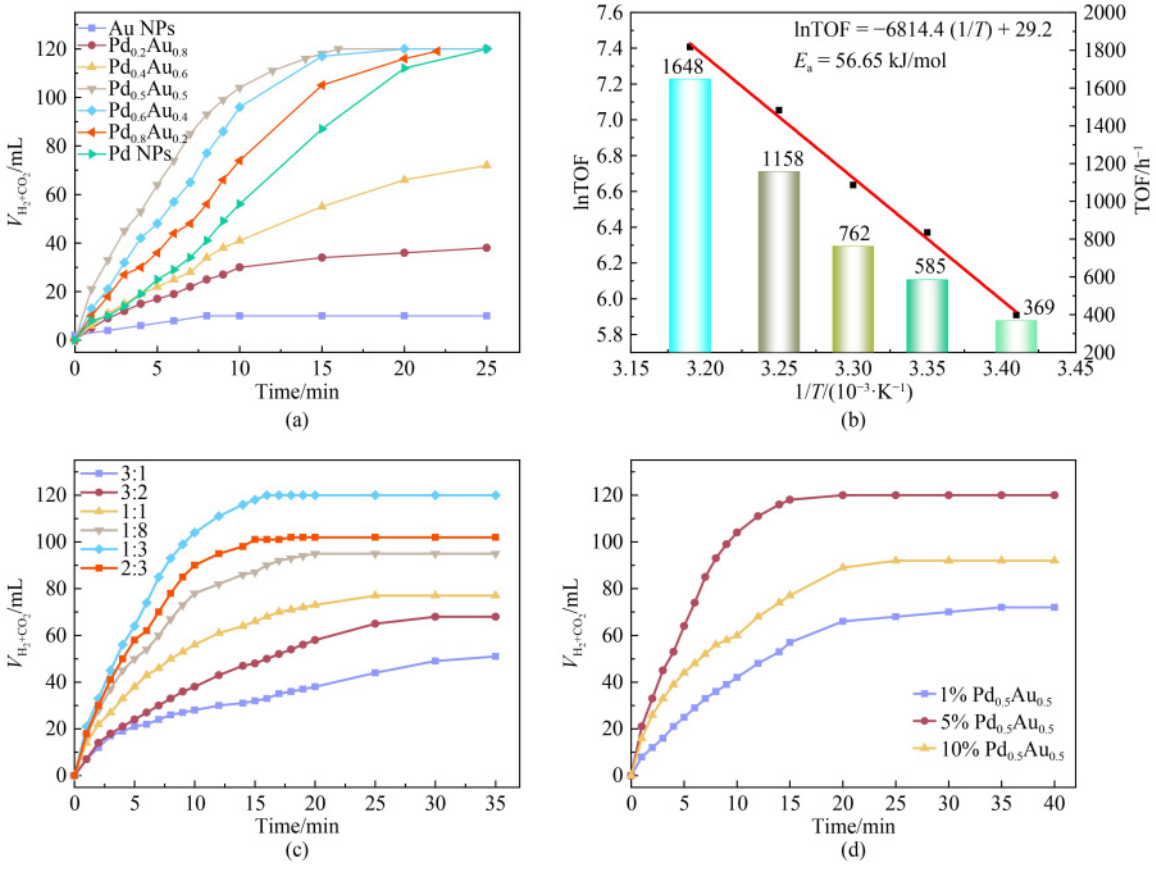

Fig. 7 Diagram of FA dehydrogenation using PdAu alloys.

(a) $V_{H_2+CO_2}$ generated versus time for dehydrogenation of FA in FA/SF solution over PdAu alloy NPs (313 K, n_{Pd+Au}/n_{FA} = 0.01, n_{FA}/n_{SF} = 1:3); (b) arrhenius plot and corresponding kinetic parameters over $Pd_{0.5}Au_{0.5}$ catalyst; (c) $V_{H_2+CO_2}$ generated versus time for dehydrogenation of FA in FA/SF aqueous solution over $Pd_{0.5}Au_{0.5}$ with different concentrations of FA/SF (313 K, n_{Pd+Au}/n_{FA} = 0.01); (d) $V_{H_2+CO_2}$ generated versus time for dehydrogenation in FA/SF aqueous solution over x% $Pd_{0.5}Au_{0.5}$ with different PdAu loadings (313 K, n_{Pd+Au}/n_{FA} = 0.01, n_{FA}/n_{SF} = 1:3).

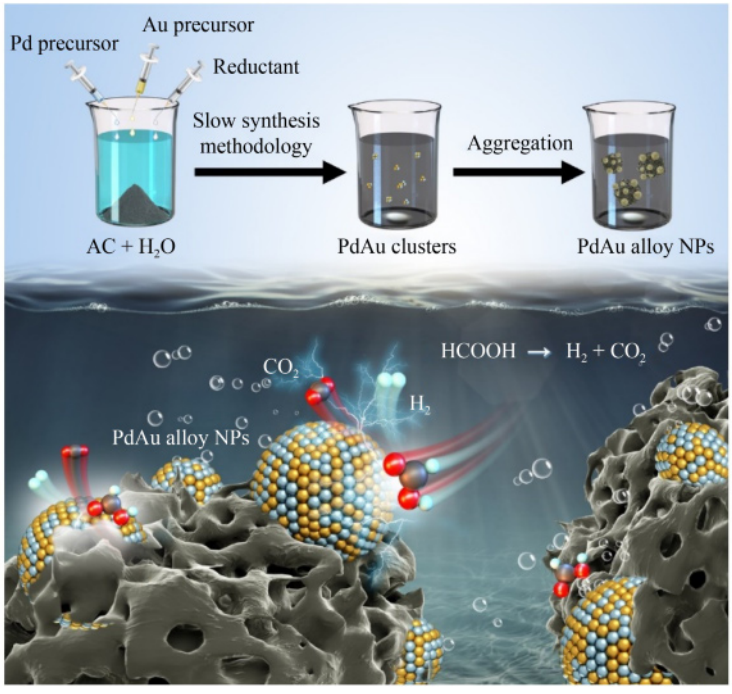

Fig. 8 Schematic diagram of FA dehydrogenation over PdAu alloy NPs obtained.

the Arrhenius equation, the E_a of $Pd_{0.5}Au_{0.5}$ is calculated at 56.65 kJ/mol lower than that of Pd NPs at 64.66 kJ/mol. As displayed in Fig. 8, the superior catalytic performance of the $Pd_{0.5}Au_{0.5}$ alloys can be ascribed to the well-distribution of bimetal active sites and synergy effect between Pd and Au that reduce activation energy obviously and boost FA decomposition.

3.6 Recyclability of optimized $Pd_{0.5}Au_{0.5}$ catalyst for FA dehydrogenation

As shown in Fig. 9, the stability and recyclability of $Pd_{0.5}Au_{0.5}$ for FA decomposition at 313 K were also measured. Although the gas produced slightly decreased, the complete conversion of the $Pd_{0.5}Au_{0.5}$ catalyst was still maintained after 5 cycles, thus displaying a high stability of $Pd_{0.5}Au_{0.5}$ catalyst. The STEM EDX mappings of Pd and Au were conducted to show the catalysts recovered after 5 cycles (Fig. 10). Before and after the catalytic decomposition of FA, there exists no significant change in size and morphology of $Pd_{0.5}Au_{0.5}$ alloy NPs, indicating the excellent structure stability of the catalyst.

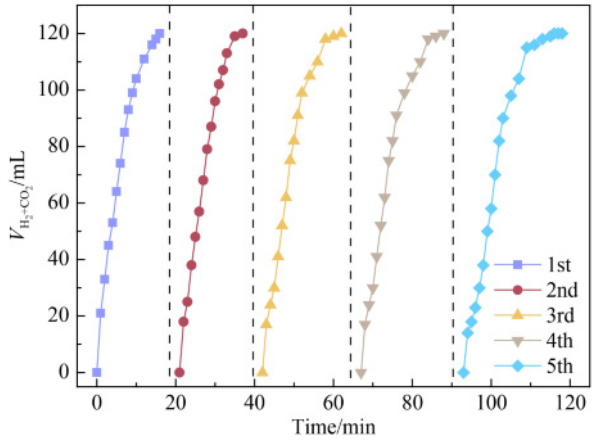

Fig. 9 Stability of optimized $Pd_{0.5}Au_{0.5}$ alloy catalyst for dehydrogenation of FA in FA/SF aqueous solution (313 K, $n_{Pd+Au}/n_{FA} = 0.01$, $n_{FA}/n_{SF} = 1{:}3$).

4 Conclusions

In this study, Pd_xAu_{1-x} (x = 0, 0.2, 0.4, 0.5, 0.6, 0.8, 1) alloy NPs over the whole composition range with various metal loading (x = 1, 5, 10 wt.%) were synthesized via a facile slow synthesis methodology. As support, the AC with large specific surface areas enlarge the polydispersity of PdAu alloys. In all PdAu alloy NPs, the as-synthesized $Pd_{0.5}Au_{0.5}$ showed the best activity, stability and recyclability for H_2 production in FA/SF mixed solution at 313 K, affording an excellent initial TOF value of up to 1648 h^{-1} with a lower E_a (56.65 kJ/mol). The optimal activity of $Pd_{0.5}Au_{0.5}$ was mainly due to the ultra-small alloy NPs, particle size polydispersity, and uniform mixing states of Pd and Au. The catalyst was also confirmed to catalyze FA dehydrogenation near room temperature, which could encourage the wide utilization of FA as one of the prospective recyclable liquidus H_2 storage materials.

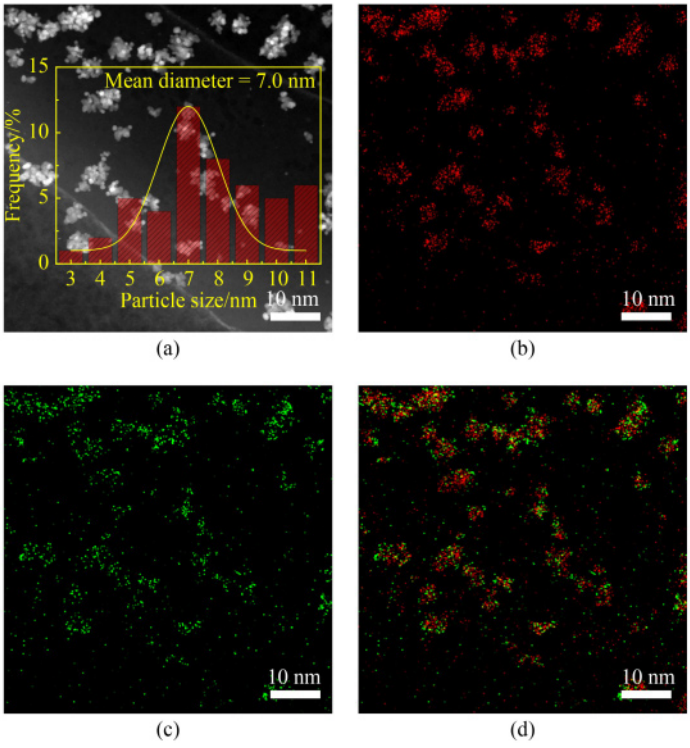

Fig. 10 HAADF-STEM images and corresponding STEM EDX maps

(a) HAADF-STEM image of $Pd_{0.5}Au_{0.5}$ after 5th reusability test; (b) corresponding STEM EDX map of Pd-L; (c) corresponding STEM EDX map of Au-L; (d) corresponding STEM EDX map of overlay images.

Acknowledgements This work was supported by the National Natural Science Foundation of China (Grant Nos. 52176131 and 51888103), the Natural Science Foundation of Shaanxi Province, China (Grant Nos. 2021JLM-18, 2020JC-04, and 2023KXJ-228), the National Science and Technology Major Project of China (No. J2019-III-0018-0062), and Xi'an Jiaotong University Special Research Project for Basic Research Business Expenses (No. xzy022022043).

Competing interests The authors declare that they have no competing interests.

References

1. Peplow M. Hydrogen economy looks out of reach. Nature, 2004, https://doi.org/10.1038/news041004-13
2. Singh S K, Zhang X B, Xu Q. Room-temperature hydrogen generation from hydrous hydrazine for chemical hydrogen storage. Journal of the American Chemical Society, 2009, 131(29): 9894–9895
3. Scofield M E, Liu H, Wong S S. A concise guide to sustainable PEMFCs: Recent advances in improving both oxygen reduction catalysts and proton exchange membranes. Chemical Society Reviews, 2015, 44(16): 5836–5860
4. Li S J, Zhou Y T, Kang X, et al. A simple and effective principle for a rational design of heterogeneous catalysts for dehydrogenation of formic acid. Advanced Materials, 2019, 31(15): 1806781
5. Wang W, He T, Yang X, et al. General synthesis of amorphous PdM (M = Cu, Fe, Co, Ni) alloy nanowires for boosting HCOOH dehydrogenation. Nano Letters, 2021, 21(8): 3458–3464
6. Yadav M, Xu Q. Liquid-phase chemical hydrogen storage materials. Energy & Environmental Science, 2012, 5(12): 9698
7. Grad O, Mihet M, Dan M, et al. Au/reduced graphene oxide composites: Eco-friendly preparation method and catalytic applications for formic acid dehydrogenation. Journal of Materials Science, 2019, 54(9): 6991–7004
8. Nielsen M, Alberico E, Baumann W, et al. Low-temperature aqueous-phase methanol dehydrogenation to hydrogen and carbon dioxide. Nature, 2013, 495(7439): 85–89
9. Yi N, Saltsburg H, Flytzani-Stephanopoulos M. Hydrogen production by dehydrogenation of formic acid on atomically dispersed gold on Ceria. ChemSusChem, 2013, 6(5): 816–819
10. Shen J, Chen W, Lv G, et al. Hydrolysis of NH_3BH_3 and $NaBH_4$ by graphene quantum dots-transition metal nanoparticles for highly effective hydrogen evolution. International Journal of Hydrogen Energy, 2021, 46(1): 796–805
11. Wang Y, Liu X. Catalytic hydrolysis of sodium borohydride for hydrogen production using magnetic recyclable $CoFe_2O_4$-modified transition-metal nanoparticles. ACS Applied Nano Materials, 2021, 4(10): 11312–11320
12. Zhang Z, Lu Z, Tan H, et al. CeO_x-modified RhNi nanoparticles grown on rGO as highly efficient catalysts for complete hydrogen generation from hydrazine borane and hydrazine. Journal of Materials Chemistry. A, Materials for Energy and Sustainability, 2015, 3(46): 23520–23529
13. Hong X, Yao Q, Huang M, et al. Bimetallic NiIr nanoparticles supported on lanthanum oxy-carbonate as highly efficient

catalysts for hydrogen evolution from hydrazine borane and hydrazine. Inorganic Chemistry Frontiers, 2019, 6(9): 2271–2278
14. Jiang Y, Kang Q, Zhang J, et al. High-performance nickel–platinum nanocatalyst supported on mesoporous alumina for hydrogen generation from hydrous hydrazine. Journal of Power Sources, 2015, 273: 554–560
15. Dai H, Qiu Y, Dai H, et al. A study of degradation phenomenon of Ni–Pt/CeO_2 catalyst towards hydrogen generation from hydrous hydrazine. International Journal of Hydrogen Energy, 2017, 42(26): 16355–16361
16. Huang W, Liu X. The "on–off" switch for on-demand H_2 evolution from hydrous hydrazine over Ni_8Pt_1/C nano-catalyst. Fuel, 2022, 315: 123210
17. Zheng J, Zhou H, Wang C, et al. Current research progress and perspectives on liquid hydrogen rich molecules in sustainable hydrogen storage. Energy Storage Materials, 2021, 35: 695–722
18. Wang Y, Liu X. Enhanced catalytic performance of cobalt ferrite by a facile reductive treatment for H_2 release from ammonia borane. Journal of Molecular Liquids, 2021, 343: 117697
19. Sun Q, Wang N, Xu Q, et al. Nanopore-supported metal nanocatalysts for efficient hydrogen generation from liquid-phase chemical hydrogen storage materials. Advanced Materials, 2020, 32(44): 2001818
20. Yang L, Hua X, Su J, et al. Highly efficient hydrogen generation from formic acid-sodium formate over monodisperse AgPd nanoparticles at room temperature. Applied Catalysis B: Environmental, 2015, 168–169: 423–428
21. Gao Y, Hu E, Yin G, et al. Pd nanoparticles supported on CeO_2 nanospheres as efficient catalysts for dehydrogenation from additive-free formic acid at low temperature. Fuel, 2021, 302: 121142
22. Suh M P, Park H, Prasad T, et al. Hydrogen storage in metal–organic frameworks. Chemical Reviews, 2012, 112(2): 782–835
23. Lee H, Kang D, Pyen S, et al. Production of H_2-free CO by decomposition of formic acid over ZrO_2 catalysts. Applied Catalysis A, General, 2017, 531: 13–20
24. Faroldi B M, Conesa J M, Guerrero-Ruiz A, et al. Efficient nickel and copper-based catalysts supported on modified graphite materials for the hydrogen production from formic acid decomposition. Applied Catalysis A, General, 2022, 629: 118419
25. Lyu Y, Xie J, Wang D, et al. Review of cell performance in solid oxide fuel cells. Journal of Materials Science, 2020, 55(17): 7184–7207
26. Wei K, Wang X, Budiman R, et al. Progress in Ni-based anode materials for direct hydrocarbon solid oxide fuel cells. Journal of Materials Science, 2018, 53(12): 8747–8765
27. Bielinski E A, Lagaditis P O, Zhang Y, et al. Lewis acid-assisted formic acid dehydrogenation using a pincer-supported iron catalyst. Journal of the American Chemical Society, 2014, 136(29): 10234–10237
28. Deng M, Ma J, Liu Y, et al. Pd nanoparticles confined in pure Silicalite-2 zeolite with enhanced catalytic performance for the dehydrogenation of formic acid at room temperature. Fuel, 2023, 333: 126466
29. Mori K, Dojo M, Yamashita H. Pd and Pd–Ag nanoparticles within a macroreticular basic resin: An efficient catalyst for hydrogen production from formic acid decomposition. ACS Catalysis, 2013, 3(6): 1114–1119
30. Peng W, Liu S, Li X, et al. Robust hydrogen production from HCOOH over amino-modified KIT-6-confined PdIr alloy nanoparticles. Chinese Chemical Letters, 2022, 33(3): 1403–1406
31. Bulushev D, Beloshapkin S, Plyusnin P, et al. Vapour phase formic acid decomposition over PdAu/γ-Al_2O_3 catalysts: Effect of composition of metallic particles. Journal of Catalysis, 2013, 299: 171–180
32. Nasiri R, Gholipour B, Nourmohammadi M, et al. Mesoporous hybrid organosilica for stabilizing Pd nanoparticles and aerobic alcohol oxidation through Pd hydride (Pd–H_2) species. International Journal of Hydrogen Energy, 2023, 48(17): 6488–6498
33. Alamgholiloo H, Rostamnia S, Hassankhani A, et al. Formation and stabilization of colloidal ultra-small palladium nanoparticles on diamine-modified Cr-MIL-101: Synergic boost to hydrogen production from formic acid. Journal of Colloid and Interface Science, 2020, 567: 126–135
34. Doustkhah E, Rostamnia S, Imura M, et al. Thiourea bridged periodic mesoporous organosilica with ultra-small Pd nanoparticles for coupling reactions. RSC Advances, 2017, 7(89): 56306–56310
35. Ahadi A, Rostamnia S, Panahi P, et al. Palladium comprising dicationic bipyridinium supported periodic mesoporous organosilica (PMO): Pd@Bipy–PMO as an efficient hybrid catalyst for Suzuki–Miyaura cross-coupling reaction in water. Catalysts, 2019, 9(2): 140
36. Farajzadeh M, Alamgholiloo H, Nasibipour F, et al. Anchoring Pd-nanoparticles on dithiocarbamate-functionalized SBA-15 for hydrogen generation from formic acid. Scientific Reports, 2020, 10(1): 18188
37. Yang Y, Xu H, Cao D, et al. Hydrogen production via efficient formic acid decomposition: Engineering the surface structure of Pd-based alloy catalysts by design. ACS Catalysis, 2019, 9(1): 781–790
38. Wang Z, Liang S, Meng X, et al. Ultrasmall PdAu alloy nanoparticles anchored on amine-functionalized hierarchically porous carbon as additive-free catalysts for highly efficient dehydrogenation of formic acid. Applied Catalysis B: Environmental, 2021, 291: 120140
39. Gu X, Lu Z, Jiang H, et al. Synergistic catalysis of metal–organic framework-immobilized Au–Pd nanoparticles in dehydrogenation of formic acid for chemical hydrogen storage. Journal of the American Chemical Society, 2011, 133(31): 11822–11825
40. Pritchard J, Kesavan L, Piccinini M, et al. Direct synthesis of hydrogen peroxide and benzyl alcohol oxidation using Au−Pd catalysts prepared by sol immobilization. Langmuir, 2010, 26(21): 16568–16577
41. Al-Nayili A, Albdiry M. AuPd bimetallic nanoparticles supported on reduced graphene oxide nanosheets as catalysts for hydrogen generation from formic acid under ambient temperature. New Journal of Chemistry, 2021, 45(22): 10040–10048
42. Sanchez F, Bocelli L, Motta D, et al. Preformed Pd-based nanoparticles for the liquid phase decomposition of formic acid:

Effect of stabiliser, support and Au–Pd ratio. Applied Sciences, 2020, 10(5): 1752

43. Dong A, Jiang Q, Zhou Y. Au_3Pd_1 intermetallic compound as single atom catalyst for formic acid decomposition with highly hydrogen selectivity. International Journal of Hydrogen Energy, 2023, 48(76): 29542–29551
44. Barlocco I, Capelli S, Lu X, et al. Disclosing the role of gold on palladium—Gold alloyed supported catalysts in formic acid decomposition. ChemCatChem, 2021, 13(19): 4210–4222
45. Feng C, Wang Y, Gao S, et al. Hydrogen generation at ambient conditions: AgPd bimetal supported on metal–organic framework derived porous carbon as an efficient synergistic catalyst. Catalysis Communications, 2016, 78: 17–21
46. Dai H, Xia B, Wen L, et al. Synergistic catalysis of AgPd@ZIF-8 on dehydrogenation of formic acid. Applied Catalysis B: Environmental, 2015, 165: 57–62
47. Gholipour B, Zonouzi A, Shokouhimehr M, et al. Integration of plasmonic AgPd alloy nanoparticles with single-layer graphitic carbon nitride as Mott-Schottky junction toward photo-promoted H_2 evolution. Scientific Reports, 2022, 12(1): 13583
48. Feng T, Wang J, Gao S, et al. Covalent triazine frameworks supported CoPd nanoparticles for boosting hydrogen generation from formic acid. Applied Surface Science, 2019, 469: 431–436
49. Cheng J, Gu X, Liu P, et al. Controlling catalytic dehydrogenation of formic acid over low-cost transition metal-substituted AuPd nanoparticles immobilized by functionalized metal–organic frameworks at room temperature. Journal of Materials Chemistry. A, Materials for Energy and Sustainability, 2016, 4(42): 16645–16652
50. Cao N, Tan S, Luo W, et al. Ternary CoAgPd nanoparticles confined inside the pores of MIL-101 as efficient catalyst for dehydrogenation of formic acid. Catalysis Letters, 2016, 146(2): 518–524
51. Yan J, Wang Z, Gu L, et al. AuPd–MnO_x/MOF–graphene: An efficient catalyst for hydrogen production from formic acid at room temperature. Advanced Energy Materials, 2015, 5(10): 1500107
52. Jin M, Oh D, Park J, et al. Mesoporous silica supported Pd-MnO_x catalysts with excellent catalytic activity in room-temperature formic acid decomposition. Scientific Reports, 2016, 6(1): 33502
53. Sun X, Ding Y, Feng G, et al. Carbon bowl-confined subnanometric palladium-gold clusters for formic acid dehydrogenation and hexavalent chromium reduction. Journal of Colloid and Interface Science, 2023, 645: 676–684
54. Luo Y, Yang Q, Nie W Y, et al. Anchoring IrPdAu nanoparticles on NH_2-SBA-15 for fast hydrogen production from formic acid at room temperature. ACS Applied Materials & Interfaces, 2020, 12(7): 8082–8090
55. Zhong H, Iguchi M, Chatterjee M, et al. Formic acid-based liquid organic hydrogen carrier system with heterogeneous catalysts. Advanced Sustainable Systems, 2018, 2(2): 1700161
56. Zhong H, Iguchi M, Chatterjee M, et al. Interconversion between CO_2 and HCOOH under basic conditions catalyzed by PdAu nanoparticles supported by amine-functionalized reduced graphene oxide as a dual catalyst. ACS Catalysis, 2018, 8(6): 5355–5362
57. Szumełda T, Drelinkiewicz A, Lalik E, et al. Carbon-supported $Pd_{100-X}Au_X$ alloy nanoparticles for the electrocatalytic oxidation of formic acid: Influence of metal particles composition on activity enhancement. Applied Catalysis B: Environmental, 2018, 221: 393–405
58. Tedsree K, Li T, Jones S, et al. Hydrogen production from formic acid decomposition at room temperature using a Ag-Pd core-shell nanocatalyst. Nature Nanotechnology, 2011, 6(5): 302–307
59. Zhao X, Xu D, Liu K, et al. Remarkable enhancement of PdAg/rGO catalyst activity for formic acid dehydrogenation by facile boron-doping through $NaBH_4$ reduction. Applied Surface Science, 2020, 512: 145746
60. Zhao X, Dai P, Xu D, et al. Ultrafine palladium nanoparticles anchored on NH_2-functionalized reduced graphene oxide as efficient catalyst towards formic acid dehydrogenation. International Journal of Hydrogen Energy, 2020, 45(55): 30396–30403
61. Kusada K, Wu D, Nanba Y, et al. Highly stable and active solid-solution-alloy three-way catalyst by utilizing configurational-entropy effect. Advanced Materials, 2021, 33(16): 2005206
62. Zhang Q, Kusada K, Wu D, et al. Solid-solution alloy nanoparticles of a combination of immiscible Au and Ru with a large gap of reduction potential and their enhanced oxygen evolution reaction performance. Chemical Science, 2019, 10(19): 5133–5137
63. Zhang Q, Kusada K, Wu D, et al. Selective control of fcc and hcp crystal structures in Au-Ru solid-solution alloy nanoparticles. Nature Communications, 2018, 9(1): 510
64. Deng C, Li Y, Sun W, et al. Supported AuPd nanoparticles with high catalytic activity and excellent separability based on the magnetic polymer carriers. Journal of Materials Science, 2019, 54(17): 11435–11447
65. Huang B, Kobayashi H, Yamamoto T, et al. Solid-solution alloying of immiscible Ru and Cu with enhanced CO oxidation activity. Journal of the American Chemical Society, 2017, 139(13): 4643–4646
66. Zhang Z J, Zhang S L, Yao Q L, et al. Metal–organic framework immobilized RhNi alloy nanoparticles for complete H_2 evolution from hydrazine borane and hydrous hydrazine. Inorganic Chemistry Frontiers, 2018, 5(2): 370–377
67. Gao S, Wang L, Li H, et al. Core–shell PdAu nanocluster catalysts to suppress sulfur poisoning. Physical Chemistry Chemical Physics, 2021, 23(28): 15010–15019
68. Scott R, Wilson O, Oh S, et al. Bimetallic palladium-gold dendrimer-encapsulated catalysts. Journal of the American Chemical Society, 2004, 126(47): 15583–15591
69. Zhu C, Guo S, Dong S. PdM (M = Pt, Au) bimetallic alloy nanowires with enhanced electrocatalytic activity for electro-oxidation of small molecules. Advanced Materials, 2012, 24(17): 2326–2331
70. Tan Z, Haneda M, Kitagawa H, et al. Slow synthesis methodology-directed immiscible octahedral Pd_xRh_{1-x} dual-atom-site catalysts for superior three-way catalytic activities over Rh. Angewandte Chemie International Edition, 2022, 61(23): 202202588
71. Chu P K, Li L H. Characterization of amorphous and

nanocrystalline carbon films. Materials Chemistry and Physics, 2006, 96(2–3): 253–277

72. Zhang A, Xia J, Yao Q, et al. Pd–WO heterostructures immobilized by MOFs-derived carbon cage for formic acid dehydrogenation. Applied Catalysis B: Environmental, 2022, 309: 121278
73. Zhang B, Su D. Probing the metal-support interaction in carbon-supported catalysts by using electron microscopy. ChemCatChem, 2015, 7(22): 3639–3645
74. Guerrero-Ortega L, Ramírez-Meneses E, Cabrera-Sierra R, et al. Pd and Pd@PdO core–shell nanoparticles supported on Vulcan carbon XC-72R: Comparison of electroactivity for methanol electro-oxidation reaction. Journal of Materials Science, 2019, 54(21): 13694–13714
75. Nowicka E, Althahban S, Luo Y, et al. Highly selective PdZn/ZnO catalysts for the methanol steam reforming reaction. Catalysis Science & Technology, 2018, 8(22): 5848–5857
76. Costa L, Vasconcelos S, Pinto A, et al. Rh/CeO_2 catalyst preparation and characterization for hydrogen production from ethanol partial oxidation. Journal of Materials Science, 2008, 43(2): 440–449
77. Jiang K, Xu K, Zou S, et al. B-doped Pd catalyst: Boosting room-temperature hydrogen production from formic acid-formate solutions. Journal of the American Chemical Society, 2014, 136(13): 4861–4864